

UCRL-JRNL-232549



LAWRENCE  
LIVERMORE  
NATIONAL  
LABORATORY

# A Proposal for High-resolution X-ray Imaging of Intermodal Cargo Containers for Fissionable Materials

B. Pohl, S. Prussin, J. Hall, J. Trebes, M.A.  
Descalle, B.J. Quiter

July 6, 2007

Journal of Applied Physics

## **Disclaimer**

---

This document was prepared as an account of work sponsored by an agency of the United States Government. Neither the United States Government nor the University of California nor any of their employees, makes any warranty, express or implied, or assumes any legal liability or responsibility for the accuracy, completeness, or usefulness of any information, apparatus, product, or process disclosed, or represents that its use would not infringe privately owned rights. Reference herein to any specific commercial product, process, or service by trade name, trademark, manufacturer, or otherwise, does not necessarily constitute or imply its endorsement, recommendation, or favoring by the United States Government or the University of California. The views and opinions of authors expressed herein do not necessarily state or reflect those of the United States Government or the University of California, and shall not be used for advertising or product endorsement purposes.



44 found in a sampling of cargo containers has been reported by Descalle, Manatt and Slaughter  
45 (ref. 3). The averaged density was found to be  $\sim 0.2 \text{ g cm}^{-3}$  with less than  $\sim 2\%$  at the theoretical  
46 maximum density of  $\sim 0.65 \text{ g cm}^{-3}$ . The fraction of all cargos with averaged densities  $\geq 0.4 \text{ g}$   
47  $\text{cm}^{-3}$  was about 10%. Because of the known real densities of materials such as ceramics, stone  
48 products, iron and steel, organic chemicals and foodstuffs, a substantial fraction of cargos  
49 through which interrogating radiation must penetrate will have densities  $\geq 1 \text{ g cm}^{-3}$ .

50  
51 At the present time, the only practical method for rapid screening of large cargo containers  
52 without significant activation of a cargo is by radiographic techniques using readily-available  
53 bremsstrahlung sources (see, e.g., ref. 4). Because of the need for high penetrability, such  
54 sources will likely have endpoint energies of  $E \geq 6 \text{ MeV}$ . The Department of Homeland Security  
55 of the United States of America (DHS) is now developing the Cargo Advanced Automated  
56 Radiography System (CAARS) for general-purpose screening of all containers. Such a system  
57 must, among other requirements, be sufficiently sensitive that it can detect cubes of high atomic  
58 number elemental material ( $Z \geq 72$ ) at normal densities and with a volume of  $100 \text{ cm}^3$  behind up  
59 to 10 in. (25.4 cm) of steel anywhere in the container (ref. 5). The CAARS specifications  
60 provide that the probability for false negative signals for this case must be no more than 1 in 60  
61 and the probability for false positive signals must be no more than 1 in 200. A  $100 \text{ cm}^3$  volume  
62 would contain  $\sim 2 \text{ kg}$  of uranium or plutonium metal. No requirements have yet been set for  
63 determining the presence of objects of arbitrary size and shape.

64  
65 Even without considering the detection of arbitrary objects of high atomic number, the  
66 difficulties in approaching the CAARS requirements are formidable. The nominal dimensions of  
67 a standard intermodal cargo container are 6 - 12 m (length) x 2.4 m (height and width). Because  
68 the materials in commerce that control the average content of most cargos are composed of  
69 elements with atomic numbers  $Z \leq 30$ , the mass attenuation coefficients for photons with  
70 energies in the range  $\sim 3 - 9 \text{ MeV}$  are all very similar and can be approximated as  $\sim 0.032 \text{ cm}^2 \text{ g}^{-1}$   
71 for scaling purposes (ref. 6). They are dominated by the contribution from incoherent scattering.  
72 At the maximum cargo loading, the average density is  $\sim 0.6 \text{ g cm}^{-3}$ , and the fraction of incident  
73 photons in this energy range that penetrate uncollided through the nominal width of a  
74 homogeneously-filled container is  $\sim 6 \times 10^{-3}$ , the fraction that would penetrate 25.4 cm of steel  
75 uncollided is  $\sim 1.9 \times 10^{-3}$ , and the fraction that would penetrate both the 25.4 cm of steel and a  
76 4.64-cm thick cube of uranium is  $\sim 3.6 \times 10^{-5}$ .

77  
78 These estimates demonstrate not only that the total attenuation is expected to be very large but  
79 also, by inference, the majority of photons emerging from the container will have suffered at  
80 least one scattering event. For example, Monte Carlo simulations of the irradiation of the  
81 homogeneously-filled container considered above with a narrow 9-MeV endpoint  
82 bremsstrahlung beam (see below) show that the intensity of events from scattered photons in a  
83 thick detector, even with an energy discriminator level ( $E_d$ ) of 3 MeV, is about 3 times that  
84 expected from uncollided photons alone. In the presence of an additional 25.4 cm of steel, the  
85 intensity of detected scattered events with  $E_d \geq 3 \text{ MeV}$  is about 8 times that from uncollided  
86 photons. Thus, under a significant range of conditions expected to be found in practice, the  
87 intensity of uncollided photons that carry the spatial information needed for localization of an  
88 object of interest and for defining its attenuating characteristics will be carried by but a small  
89 fraction of the radiation emanating to a detector. While correction for scattered photons is not at

90 all new to radiography, the magnitude of the scattered intensity expected in cargo interrogation  
91 far exceeds that normally met with in medical and most industrial applications. We have found  
92 no publication in the open or patent literature that directly addresses this problem.

93  
94 In this manuscript, we wish to demonstrate that the simple physics of Compton scattering,  
95 combined with the slowing down characteristics of highly-relativistic electrons and the general  
96 properties of the most cargos, may provide a path for development of an effective and sensitive  
97 screening mechanism for actinides in elemental form. Further, because of the relatively low total  
98 dose that must be delivered to a cargo, a procedure might be developed that is not life  
99 threatening to stowaways and allows for tomography of reasonable order in cases where such an  
100 approach would be advantageous. Because the dimensions of an object must be known if an  
101 attenuation coefficient is to be extracted, we assume that at least two orthogonal views through  
102 the container will be acquired.

## 103 104 105 **2. General Theoretical Considerations**

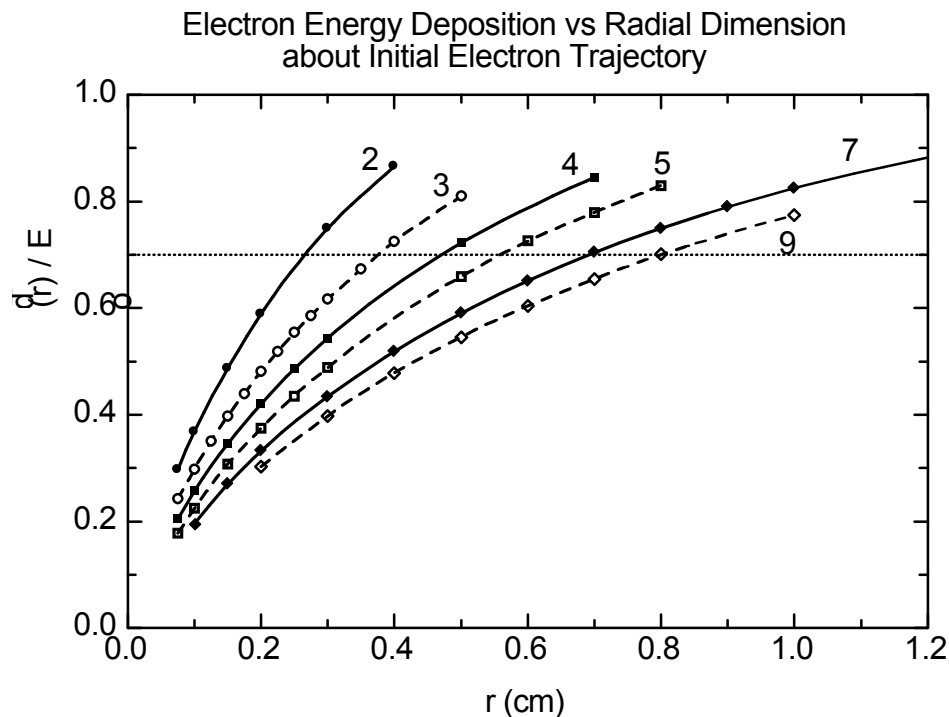
### 106 107 2.1 Photon Transport in Cargo

108  
109 Bremsstrahlung radiation with energies significantly less than  $\sim 2$  MeV will be much more  
110 strongly attenuated in the highly-attenuating media considered here than those of higher energy  
111 and thus will not contribute greatly to the photon spectrum emanating from a container. In the  
112 Compton limit, single incoherent interactions of 4-9 MeV photons result in scattered photons  
113 with energies less than 3 MeV when the photon scattering angle is  $\theta \geq 30^\circ$ , for which the  
114 fraction of total incoherent interactions is  $\geq 0.6$ . Further, and neglecting photoelectric absorption,  
115 more than 85% of the photons emerging from the homogeneously-filled container described  
116 above will have suffered at least two incoherent scattering events. Thus it is reasonable to  
117 conclude that the majority of photons emerging from the container that have suffered more than  
118 a single Compton event can be suppressed by simple energy discrimination in the range  $\sim 2$ -3  
119 MeV. With such discrimination, the resultant signal in an external detector will be due primarily  
120 to the desired uncollided photons and photons that have suffered but a single incoherent  
121 scattering. Given the general characteristics of the cargo fill that can be gleaned from the cargo  
122 manifest and weight, the fraction of the signal intensity due to single scattered photons should be  
123 easily estimated with the Compton scattering formalism. Along with the requirement that at least  
124 two orthogonal radiographs are acquired to provide an estimate of the dimensions of an object of  
125 interest, the ability to provide reasonable detection efficiency with sufficient spatial resolution  
126 for effective imaging rests on the spatial requirements for stopping of high-energy Compton  
127 electrons produced in an external detector.

### 128 129 2.2 Detector Response

130  
131 The Compton electrons from scattering of photons with energies in the range 4-9 MeV at angles  
132  $\leq 30^\circ$  are found at angles within about  $20^\circ$  of the trajectory of the incident photons. Further, for  
133 electrons with kinetic energies in the same range, the probability for undergoing large-angle  
134 scattering before losing the majority of their kinetic energy by slowing down is small.  
135 Calculations based on the Møller scattering relation (see, e.g., ref. 7) show, for example, that the

136 probability of scattering at an angle of  $20^\circ$  in the laboratory coordinate system is smaller by  
 137 factors of about 20-25 compared to electrons of energy 0.1 MeV. Thus, the majority of the  
 138 kinetic energy of most high-energy electrons produced in an external detector will be deposited  
 139 in a relatively small volume about the trajectory of the incident photon. As an example, the  
 140 fractions of total energy deposited within cylindrical volumes about the trajectories of incident  
 141 electrons are shown in Figure 1 as functions of radial dimension and initial electron kinetic  
 142 energy. These results were obtained in simulations with the code MCNP4C using the high-  
 143 resolution electron transport option (ref. 8). The detector was modeled as a common plastic  
 144 scintillator of composition  $C_{10}H_{11}$  and density of  $1.03 \text{ g cm}^{-3}$  (ref. 9). On the average, more than  
 145 70% of the electron energy is deposited within a radial dimension  $r \leq 0.8 \text{ cm}$ . This implies that  
 146  
 147



148  
 149  
 150 Figure 1. The fraction of electron kinetic energy deposited within a radial dimension  $r$   
 151 about the initial trajectory of an incident electron in a plastic detector (see text). The  
 152 numbers adjacent to the various curves are the incident electron kinetic energies in MeV.  
 153 Statistical errors in the simulations are generally within the size of the symbols.  
 154  
 155

156 the spatial resolution for interesting objects using a 9 MeV bremsstrahlung spectrum can be on  
 157 the order of  $\leq 1.5 \text{ cm}$  in such a detector. For the common scintillators  $\text{NaI(Tl)}$  or  $\text{Bi}_4\text{Ge}_3\text{O}_{12}$ , the  
 158 spatial resolution can be smaller by factors of  $\sim 1.5 - 3.0$ , respectively, owing to their larger  
 159 electron densities, although some correction must be made for bremsstrahlung losses in the case  
 160 of  $\text{Bi}_4\text{Ge}_3\text{O}_{12}$ .  
 161  
 162

### 163 3. Monte Carlo Simulations

164  
165 The methodology outlined above has been examined with schematic simulations of a number of  
166 shielded and unshielded spheres of uranium and several other test objects. For all simulations the  
167 cargo container was assumed to have the nominal dimensions given above and was filled with  
168 water at a density of  $0.6 \text{ g cm}^{-3}$ . The bremsstrahlung spectrum was modeled from a 9 MeV  
169 electron beam interacting with a 2-cm thick tungsten target centered at 208 cm from the entrance  
170 face of the container and located on its centerline. A narrow bremsstrahlung beam was taken as  
171 that emerging from a spherical surface of 37.3 cm radius surrounding the target and collimated  
172 to provide a fan beam in the vertical direction. The horizontal width of the beam at entrance to  
173 the cargo container was 1.73 cm and diverged to 3.76 cm at entrance into the detector located  
174 immediately adjacent to the opposite face of the container at a distance of 244 cm. For some  
175 simulations a wide beam 18.2-cm in width was produced by translating the narrow beam in  
176 horizontal steps of 1.5 cm.

177  
178 As discussed above, the detector was modeled as a plastic scintillator with dimensions of 50 cm  
179 (height) x 50 cm (width) and 6" (15.4 cm) thickness. Photon interactions were allowed to occur  
180 throughout the detector volume and electron transport was used to define the total energy  
181 deposited in various interaction volumes. To simulate the response of a pixilated detector, the  
182 detector surface was divided into an array of 1.5 cm x 1.5 cm areas. The energy deposited in a  
183 detector pixel was defined as that deposited in the volume swept by projecting the pixel surface  
184 through the detector. The response of a more realistic scintillator comprised of individual  
185 parallelepipeds separated by lead foils sufficiently thick to prevent transmission of electrons,  
186 scintillation light and low-energy bremsstrahlung was shown by simulations to provide  
187 essentially the same results for high energy radiations although the total count rates were  
188 reduced by about a factor of 2. The total average attenuation of 3-9 MeV photons traversing the  
189 thickness of the detector was  $\sim 0.35$ . The detector efficiency per bremsstrahlung source photon  
190 was obtained by direct comparison of the intensities in pixels in the absence of a target and with  
191 and without the water fill. This efficiency was used to normalize the results from the simulations  
192 to the results from the first Compton scatter calculations.

193  
194 The thrust of all simulations and analyses presented here is to judge the efficacy of the proposed  
195 approach for providing high-quality linear attenuation coefficients from which detection of high-  
196 Z fissionable materials can be ascertained in massive cargos. For this purpose, it is assumed that  
197 the dimensions of an object are known and that the only errors are those due to the estimated  
198 statistical errors inherent in the simulated intensities in the detector pixels.

### 199 200 3.1 Test of the Concept

201  
202 A simple test of the general concept outlined above was obtained by the simulation of a 2-cm  
203 radius totally absorbing sphere located at the center of the filled cargo container that is  
204 interrogated by the narrow bremsstrahlung beam defined above. The intensities (lineouts) of  
205 events per source photon in the vertical line of pixels passing through the centerline of the target  
206 are shown as a function of discrimination energy in Figure 2. As the threshold level is raised  
207 from 1 eV to 3 MeV, the intensity in non-target and target pixels decreases by a factor of about  
208 7-8 and 55, respectively. In Figure 3 are shown the effective linear attenuation coefficients as a  
209 function of discrimination energy as estimated in the normal manner by calculating the quantity

210

211

$$\mu_{\text{eff}} = \frac{1}{x_{\text{obj}}} \ln \frac{I'}{I} \quad (1)$$

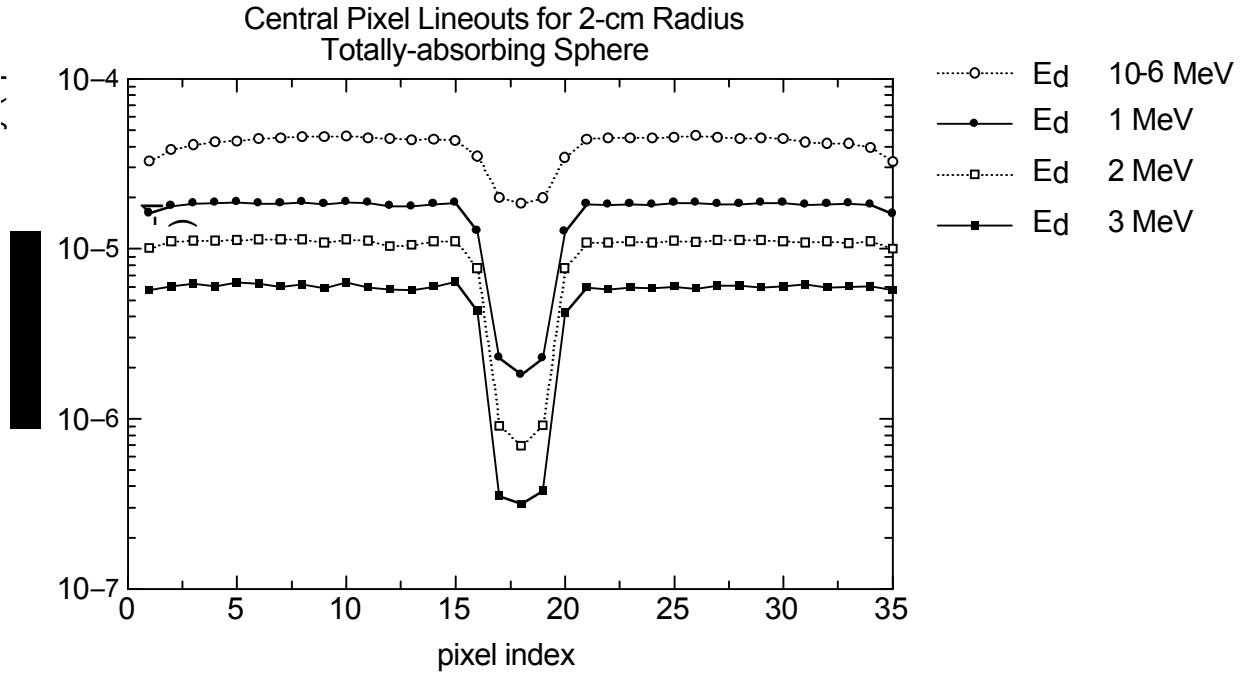
212

213 where  $I'$  is the average intensity in a non-target pixel and  $I$  is the intensity in the central target pixel.

214

215

216



217

218

219 Figure 2. Intensities (lineouts) in the vertical column of pixels along the centerline of a 2-  
220 cm radius totally absorbing sphere located at the center of cargo container filled  
221 homogeneously with water at a density of 0.6 g cm<sup>-3</sup>.

222

223 The calculated  $\mu_{\text{eff}}$  are seen to increase by a factor of about 3 as the discrimination level is  
224 raised from about 1 eV to about 3 MeV. The error bars shown represent only the 1  $\sigma$  statistical  
225 uncertainties in  $I$  and  $I'$  estimated in the Monte Carlo simulations. The lower limit indicated by  
226 the underlined arrow represents the  $\mu_{\text{eff}}$  obtained by applying the analytical estimate of the first-  
227 Compton scattering intensity with the procedure outlined in the Appendix. Within the statistical  
228 errors, the resultant  $\mu_{\text{eff}}$  is consistent with the infinite value expected.

229

230 This simple test supports the central ideas that, in the main, energy discrimination removes the  
231 majority of multiple-scattered incident photons and that the remaining scattered intensity can be  
232 estimated reasonably well from the simple physics of Compton scattering. These conclusions are  
233 further supported by analytical considerations and other simulations with the homogeneously-  
234 filled container in the absence of a target. In particular, the strong dependence of the energy of  
235 scattered photons on the scattering angle means that high-energy scattered photons reaching a



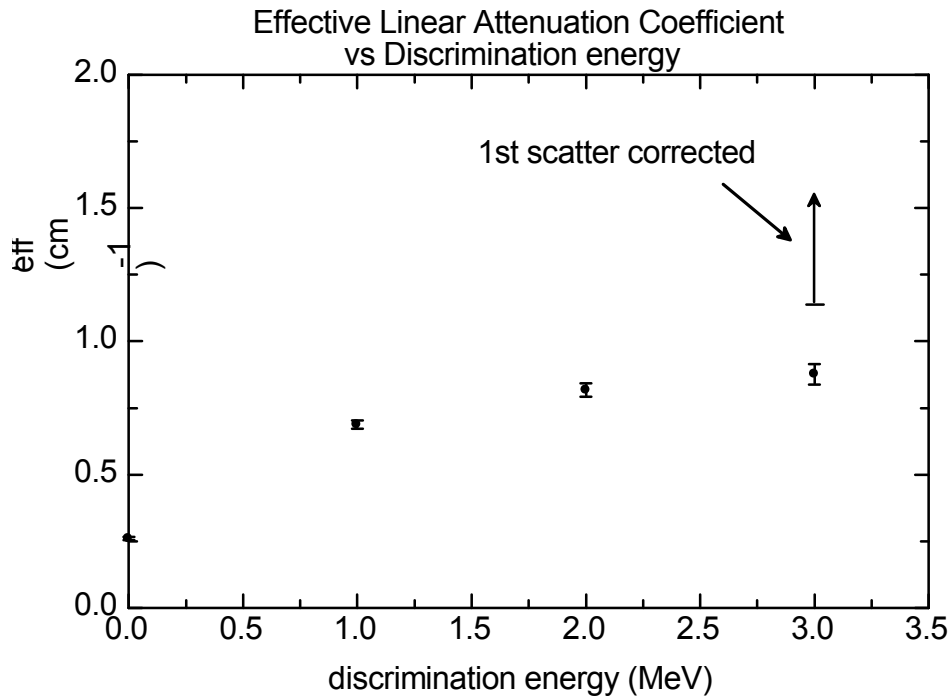


Figure 3. Effective linear attenuation coefficient,  $\mu_{\text{eff}}$ , extracted from the Monte Carlo simulations shown in Figure 2 as a function of detector discrimination level.

236  
237

238

239

240

241

242 target pixel can only arise from interactions that take place within a fairly small transverse  
243 dimension about the incident photon's trajectory.

244

245

246

247

### 3.2 Simulations of Shielded and Unshielded Uranium and Rhodium Spheres.

248 The methodology discussed here has been applied to simulations of an array of targets, including  
249 uranium spheres with radii of 1, 2 and 3 cm, a 2-cm radius uranium sphere contained within 2-  
250 cm thick spherical shells of iron and lead, and a 2-cm sphere of rhodium, the element with the  
251 largest linear attenuation coefficient outside of the actinides. The smallest uranium sphere  
252 represents a case for which the object is comparable in size to the pixel dimension while the  
253 largest uranium sphere approaches that of a totally absorbing object. The Monte Carlo  
254 simulations were performed in the same manner as described in Section 3.1, i.e., all targets were  
255 located at the center of a cargo container that was otherwise filled with water at  $0.6 \text{ g cm}^{-3}$ . In  
256 the case of the 3-cm radius sphere of uranium, the water contained in the 25.4-cm thick slab  
257 immediately adjacent to the beam entrance was replaced by the same thickness of iron in order  
258 to provide a simulation somewhat more stringent than that specified in the DHS requirements  
259 discussed in Section 1.

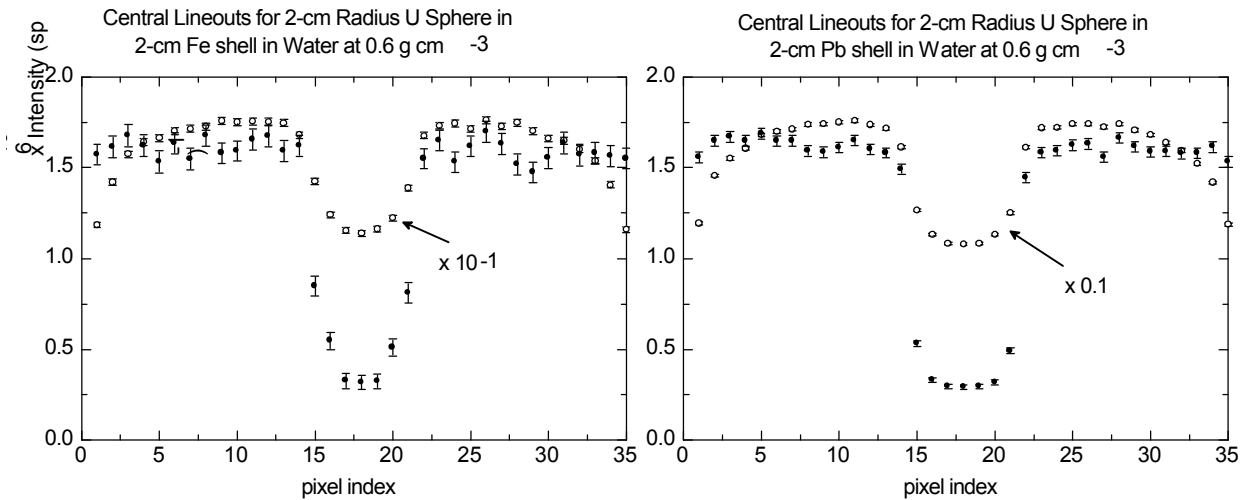
260

261 In all cases,  $\mu_{\text{eff}}$  of the object of interest was calculated from equation (1) using the simulated  
262 intensities with a 3 MeV discrimination level. The intensity  $I$  was taken as that in the central  
263 target pixel and the intensity  $I'$  was taken as the average intensity in the five non-target pixels

264 just removed from the target region, both intensities corrected for scattering above the  
 265 discriminator level with the model given in the Appendix. For simplicity, it was assumed that  
 266 the object itself was totally absorbing in applying the scattering model. With the exception of the  
 267 case of a uranium sphere shielded in a spherical shell of iron discussed further below, this  
 268 approximation is reasonable but somewhat conservative. No corrections were made for the  
 269 divergence of the bremsstrahlung beam that leads to magnification of the target in the detector  
 270 plane.

271  
 272 The total target thickness penetrated by unattenuated photons that interact in the central target  
 273 pixel was taken as the mean cord length through a sphere over the pixel width. To compare the  
 274 derived  $\mu_{\text{eff}}$  with those expected, spline fits to tabular values of  $\mu/\rho$  from ref. 6 were averaged  
 275 over the simulated bremsstrahlung spectrum in the energy range 3-9 MeV and then multiplied  
 276 by the normal density of the element. For shielded spheres, the  $\mu_{\text{eff}}$  derived in this way were  
 277 again averaged by the mean cord lengths through the spherical cores and spherical shells.

278  
 279 As examples, the intensities from the vertical columns of detector pixels that contain the central  
 280 targets pixels for simulations of a 2-cm radius sphere of uranium contained in 2-cm thick  
 281 spherical shells of iron and lead are shown in Figure 4. For these simulations the 18.2 cm wide  
 282 beam was used. In both cases, the increase in detector threshold energy from 0.1 keV to 3 MeV  
 283  
 284  
 285

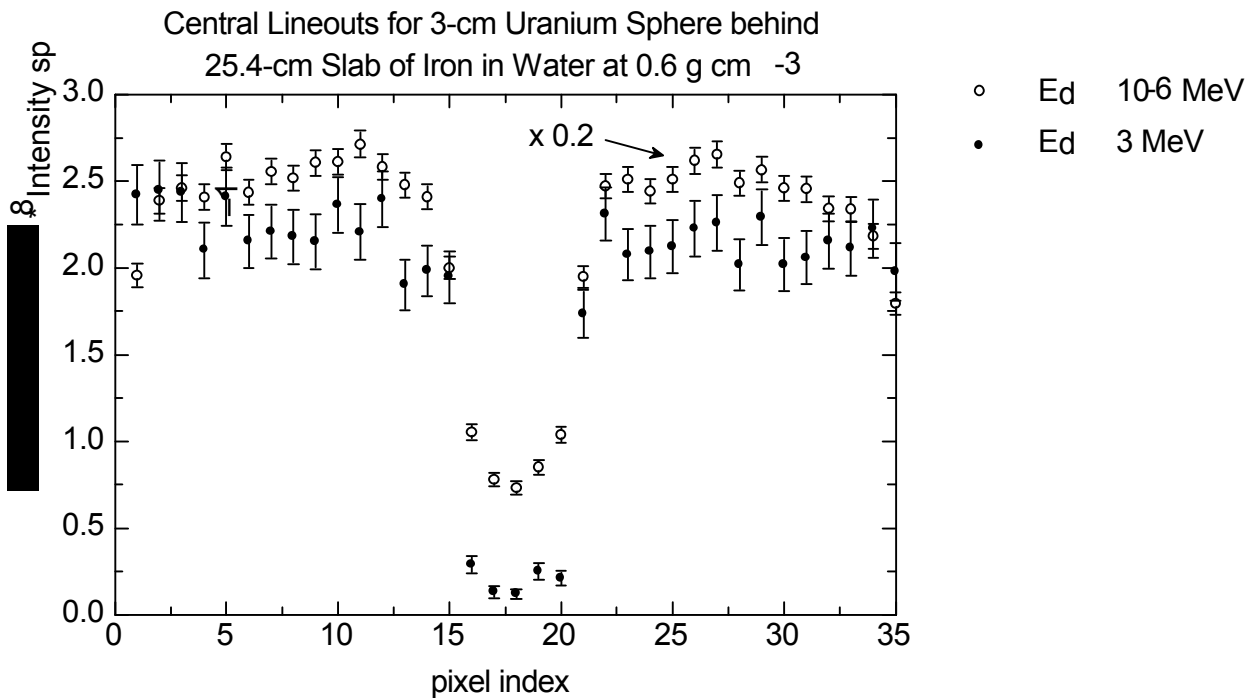


286  
 287  
 288 Figure 4. Intensities in vertical column of pixels containing the central target pixel for a  
 289 2-cm radius sphere of uranium inside of a 2-cm thick spherical shell of iron (left panel)  
 290 and inside of a 2-cm thick spherical shell of lead (right panel). The vertical axes of the  
 291 two panels are identical. Open circles - 0.1 keV detector threshold. Closed circles - 3  
 292 MeV detector threshold. Errors bars represent the estimated  $1\sigma$  statistical uncertainty in  
 293 the simulation only.

294  
 295  
 296 reduces the intensities in non-target pixels by about a factor of 10 while the intensities in the  
 297 central target pixels are reduced by about a factor of 40. Although both targets have the same

298 dimensions, that for the iron-shielded uranium sphere appears to be significantly smaller in the  
 299 vicinity of the central target pixel than that of the lead-shielded sphere due to the rather high  
 300 transparency of the outer 1 cm of the iron. Also evident is the magnification of the target in the  
 301 detector plane because of the divergence of the bremsstrahlung beam.  
 302

303 The simulation of the 3-cm radius uranium sphere in the presence of a 25.4-cm thick slab of iron  
 304 at the beam entrance to the container is shown in Figure 5. Again the wide beam was used in the  
 305 simulation. The strong attenuation by the iron slab is immediately evident, the intensities in non-  
 306 target pixels being smaller by a factor of about 130 compared to the intensities seen in Figure 4  
 307 when the detector discrimination level is 3 MeV. Nevertheless, and notwithstanding the fact that  
 308 the iron also acts as a very strong scattering source, the uranium sphere is quite well visualized.  
 309 While the statistical quality of the simulation is poorer because of computational limitations, the  
 310 ratio of the average intensity in non-target pixels to that in the central target pixels is essentially  
 311  
 312  
 313



314  
 315  
 316 Figure 5. Intensities in the vertical column of pixels containing the central target pixel for  
 317 a 3-cm radius sphere of uranium behind a 25.4-cm thick slab of iron with the remainder  
 318 of the container filled with water at a density of 0.6 g cm<sup>-3</sup>. Errors bars represent the  
 319 estimated 1σ statistical uncertainty in the simulation only.  
 320

321  
 322 identical to that seen in Figure 2 for the totally absorbing sphere as it should be. A 3-cm radius  
 323 sphere of uranium is very nearly totally absorbing to 3-9 MeV photons. This indicates, at least  
 324 qualitatively, that the addition of a strong scattering source does not greatly change the relative  
 325 intensity of high-energy photons that scatter into the target pixels.  
 326

327 A summary of the principal parameters from 7 of the simulations considered in this work is  
 328 given in Table 1 and the  $\mu_{\text{eff}}$  extracted from the simulations and the first scattering model are  
 329 compared to those expected from the attenuation properties of the target in Figure 6. As seen in  
 330 the summary and the figure, the application of energy discrimination, coupled with the first  
 331 Compton scatter estimates that assume the target to be totally absorbing, lead to linear  
 332 attenuation coefficients that agree with the expected values to within about  $1 \sigma$  except for case c.  
 333 As discussed previously (see Figure 4), the outer portion of the iron shield is relatively  
 334 transparent to the high-energy photons considered here. Simple analytical estimates show, for  
 335 example, that the transmission of the outer 1 cm of the iron to photons in the energy range 3-9  
 336 MeV is about 0.4. Because first scatterings that result in photons near the source energy are  
 337 produced only at small scattering angles, this transparency has a significant effect on the  
 338 intensity of the first scattering estimate. Indeed, an approximate calculation that includes this  
 339 transparency brings the extracted  $\mu_{\text{eff}}$  well within the  $1 \sigma$  limits of a one-to-one correspondence  
 340 with the expected value.

341  
 342  
 343 Table 1. Summary of principal parameters of 7 simulations used to test the efficacy of the  
 344 energy discrimination plus first scattering model approach.

target	thickness <sup>d</sup> (cm)	$\mu_{\text{expected}}$ (cm <sup>-1</sup> )	$\mu_{\text{eff}}$ (cm <sup>-1</sup> ) <sup>b</sup>	$\mu_{\text{eff}} / \mu_{\text{expected}}$
water cargo	244.000	0.020 <sup>c</sup>	$0.020 \pm 0.003$	$1.00 \pm 0.15$
Rh sphere (r = 2 cm)	3.369	0.467	$0.463 \pm 0.022$	$0.991 \pm 0.047$
U sphere (r = 2 cm) in 2-cm thick Fe shell <sup>a</sup>	5.333	0.549	$0.435 \pm 0.067^a$	$0.792 \pm 0.122^a$
U sphere (r = 2 cm) in 2-cm thick Pb shell	5.333	0.603	$0.524 \pm 0.079$	$0.869 \pm 0.131$
U sphere (r = 2 cm)	3.369	0.851	$0.892 \pm 0.057$	$1.048 \pm 0.067$
U sphere (r = 3 cm) + 25.4-cm thick Fe slab	4.000	0.850	$0.801 \pm 0.271$	$0.942 \pm 0.319$
U sphere (r = 1 cm)	1.684	0.851	$0.764 \pm 0.093$	$0.898 \pm 0.109$

345  
 346 <sup>a</sup> uncorrected for transparency through outer portion of the iron shell. See text.  
 347 <sup>b</sup> uncertainties due solely to estimated statistical uncertainties in the Monte Carlo intensities.  
 348 <sup>c</sup> for water at a density of  $0.6 \text{ g cm}^{-3}$ .  
 349 <sup>d</sup> mean thickness of target averaged over the dimension of the central pixel.

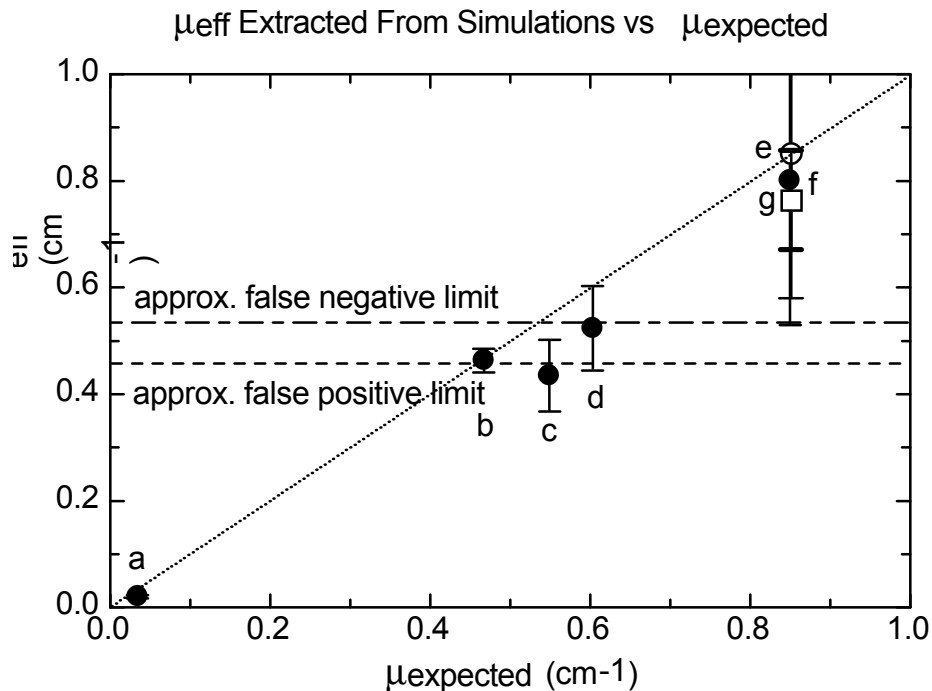
#### 352 4. Discussion

353  
 354  
 355 The simulations and analysis presented above suggests that it is indeed possible to determine the  
 356 linear attenuation coefficient of isolated objects of normal elemental density with sufficient  
 357 accuracy that a reliable and efficient screening procedure might be developed based on a single  
 358 endpoint energy bremsstrahlung beam. The fundamental issue is the ability to distinguish  
 359 between high-Z objects that might contain fissionable material and lower atomic numbers within

360 the limits for false positive and false negative signals desired by the DHS. In Figure 6 are shown  
 361 approximate limits for the false positive and false negative detection rates specified for CAARS  
 362 calculated with rough estimates of uncertainties in the attenuation coefficient of the cargo and  
 363 the dimensions of an object. With the exception of some shielding conditions, both limits might  
 364 be met with detailed development of the proposed methodology. Although not presented here, it  
 365 may be completely possible to improve the identification of high-Z objects by analysis of  
 366 various energy ranges of the detected events.

367  
 368 The majority of the simulations were performed with about  $10^8$  histories. Commercial  
 369 bremsstrahlung sources can produce roughly  $10^{12}$  photons  $s^{-1}$ . Assuming that general purpose  
 370 scanning must be accomplished in about 1 min, a 40' (12.2 m) cargo container, and a beam  
 371 width on the order of 10 cm, the maximum count rates in an individual pixel would be less than  
 372 about  $5 \times 10^4 s^{-1}$ . Such rates should permit energy discrimination in the detection system with  
 373 standard electronics and techniques. For objects such as the 3-cm radius sphere of uranium  
 374 shielded by 25.4 cm of iron, which required  $10^{10}$  histories to produce the statistical quality  
 375 shown in Figure 5, it is assumed that much longer data acquisition times will be permitted if  
 376 warranted. Further, a reasonable number of angular projections can be acquired in a relatively  
 377 short time where they might prove useful to better define the attenuation characteristics of  
 378 suspect objects in cluttered environments.

379  
 380  
 381



382  
 383  
 384 Figure 6. The  $\mu_{\text{eff}}$  extracted from the Monte Carlo simulations and the first Compton  
 385 scattering correction versus the expected linear attenuation coefficient. All simulations  
 386 assume that targets are located at the center of a cargo container otherwise filled  
 387 homogeneously with water at a density of  $0.6 \text{ g cm}^{-3}$ . Errors bars represent the estimated  
 388  $1\sigma$  statistical uncertainty in the simulation only. a- water cargo; b - Rh sphere ( $r = 2 \text{ cm}$ );

389 c - U sphere ( $r = 2$  cm) in 2-cm thick Fe shield; d - U sphere ( $r = 2$  cm) in 2-cm thick Pb  
390 shield; e - U sphere ( $r = 2$  cm); f - U sphere ( $r = 3$  cm) + 25.4-cm thick Fe slab;  
391 g - U sphere ( $r = 1$  cm).

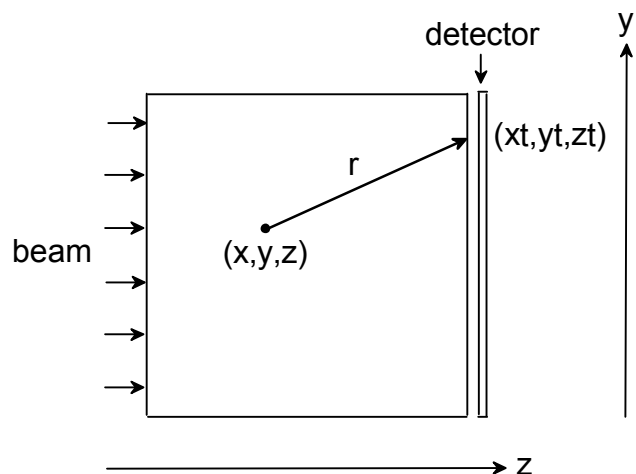
392  
393  
394 The dose that might be received by a human during scanning was estimated with a crude  
395 phantom model in the case where  $10^8$  histories were simulated. If a person were stationary in the  
396 container, the whole body dose was estimated to be roughly 200 mrad. If the individual  
397 traversed the container along with the bremsstrahlung beam, the estimated dose was about 2 rad.  
398

399 The quality of the linear attenuation coefficients estimated in this work was somewhat  
400 compromised by the simplicity of the implementation of the first scattering model. Nevertheless  
401 they should be illustrative of what might be expected in practice for isolated objects in a  
402 container with a homogeneous cargo fill. Because of the makeup of most cargos, and assuming  
403 that the cargo manifest and weight are known, it should be possible to obtain a reasonable  
404 estimate of the effective density and attenuation coefficient of the cargo from the two orthogonal  
405 radiographs assumed here. Our experience with photon transport in a similar energy range for  
406 examining the use of delayed  $\gamma$  rays for detecting fissionable materials has shown that apart from  
407 significant streaming paths, the requirement of homogeneity should not be a serious limitation.  
408 Whether cargo clutter will be a significant limitation and whether there is any hope of  
409 distinguishing non-elemental objects containing actinides still awaits study.  
410

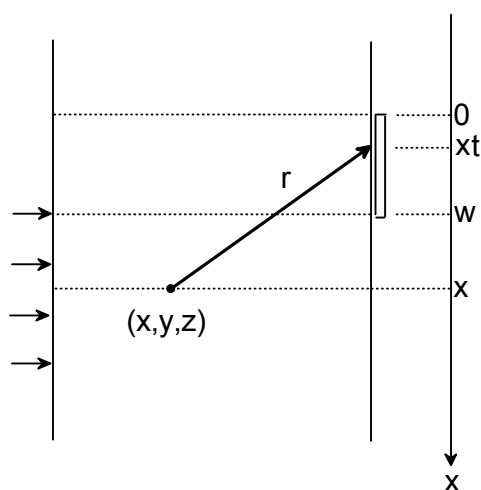
411 Finally, we wish to point out that unequivocal definition of the presence of fissionable material  
412 can be obtained by irradiation of the cargo container with higher-energy photons or with  
413 neutrons with energies  $\geq 7$  MeV by detecting high-energy  $\beta$ -delayed  $\gamma$ -ray emission. This could  
414 be attained with the same detector system as envisioned here with a dual-purpose interrogation  
415 system. This would provide a very powerful deterrence against the secretion clandestine nuclear  
416 materials in cargo containers.  
417

## 418 419 **5. Appendix: First Scattering Approximation**

420  
421 In Figure A.1 is shown a schematic of a cargo container from which the first scattering  
422 approximation is derived. The width of the container is  $z_0$ . Pixels associated with the position of  
423 an interesting object are contained within the dimension  $0 \leq x_t \leq w$ . The container is irradiated  
424 with bremsstrahlung photons incident normally on the container side opposite to the detector .  
425 We consider here only the first scatterings of bremsstrahlung photons that are incident on the  
426 detector plane over the dimension  $w \leq x \leq x_0$ .  
427



End view



Top view

Figure A.1 End and top views of the geometry used for derivation of the expression for calculating the intensity of events from single Compton scattering of monoenergetic photons incident on the cargo container volume.

Photons of intensity  $I_0 \text{ cm}^{-2}$  are incident at the location  $x, y, z = 0$ , interact at the location  $x, y, z$  by Compton scattering, and produce scattered photons that are directed along the trajectory  $r$  to a point  $x_t, y_t, z_t$  in the detector plane. The magnitude of  $r$  is  $r = \left[ (x - x_t)^2 + (y - y_t)^2 + (z - z_t)^2 \right]^{1/2}$ .

The electron density is  $n_e \text{ cm}^{-3}$  and the differential Compton collision cross section for unpolarized photons is  ${}_e\sigma_c(\theta) \text{ cm}^2 \text{ str}^{-1}$ . With normal Cartesian and polar coordinate systems, where  $\theta$  is the polar angle and  $\phi$  is the azimuthal angle, the element of solid angle between  $\theta$  and

445  $(\theta + d\theta)$  and  $\phi + (\phi + d\phi)$  is  $d\omega = \sin\theta d\theta d\phi$  and the surface area subtended by this solid angle is  
 446  $dS = r^2 d\omega$ . The total rate of scattering events from photons incident in the differential area  $dA$   
 447 about the location  $(x, y, z = 0)$  that interact between  $z$  and  $(z + dz)$  and produce photons scattered  
 448 into  $d\omega$  is

$$449 \quad n_e I_o e^{-\mu z} \sigma_C(\theta) dA_e dz d\omega \text{ s}^{-1} \quad (\text{A.1})$$

450  
 451 The flux of unattenuated first-scattered photons at the point  $(x_t, y_t, z_o)$  produced from these  
 452 events is then

$$453 \quad d\phi = \frac{e^{-\mu r}}{r^2} I_o e^{-\mu z} dA_e \sigma_C(\theta) \cos(\theta) n_e dz \text{ cm}^{-2} \text{ s}^{-1}, \quad (\text{A.2})$$

454  
 455 where the factor  $\cos(\theta)$  represents the projection of  $dS$  onto the plane surface of the detector.  
 456 The total flux of first-scattered photons per unit intensity  $I_o$  at  $(x_t, y_t, z_o)$  due to interactions along  
 457 the range  $0 \leq z \leq z_o$  is then

$$458 \quad \frac{d\phi}{I_o dA} = n_e \int_0^{z_o} \frac{e^{-\mu r}}{r^2} e^{-\mu z} \sigma_C(\theta) \cos(\theta) dz, \quad (\text{A.3})$$

459  
 460 where  $e^{-\mu r}$  accounts for attenuation of the scattered photons along the trajectory  $r$ . The energy  
 461 spectrum of the photons arriving at the detector plane is readily obtained from the normal  
 462 Compton relation

$$463 \quad E'(\theta) = \frac{E_o}{1 + \frac{E_o}{m_e c^2} (1 - \cos(\theta))}, \quad (\text{A.4})$$

464  
 465 where  $E_o$  and  $E'(\theta)$  are the energies of the incident photon and scattered photon, respectively  
 466 and  $m_e$  is the rest mass of the electron.

467  
 468 In the implementation used here, the incident photons were assumed to be normal to the face of  
 469 the cargo container and no account was taken for the divergence of the beam. Intensities of  
 470 scattered photons from incident monoenergetic photons incident over the range  $0 \leq x \leq w$  were  
 471 calculated only at the center of 1 cm x 1 cm pixels located at the front face of the detector ,  
 472 weighted for the intensity distribution of the bremsstrahlung spectrum and then normalized to  
 473 the Monte Carlo simulations by use of the simulated efficiency for photon detection. Further, it  
 474 was assumed that the target was totally absorbing and thus the first scattered intensity will be  
 475 underestimated to some extent.

481  
 482  
 483 References  
 484



- 485 1. E.B. Norman, S.G. Prussin, R-M Larimer, H. Shugart, E. Browne, A.R. Smith, R.J.  
486 McDonald, H. Nitsche, P. Gupta, M.I. Frank, T.B. Gosnell, Nucl. Instrum. & Methods A **521**  
487 (2004) 608.  
488
- 489 2. S.G. Prussin, M-A. Descalle, J.M. Hall, J.A. Pruet, D.R. Slaughter, M.R. Accatino, O.J.  
490 Alford, S.J. Asztalos, A. Bernstein, J.A. Church, T. Gosnell, A. Loshak, N.W. Madden, D.R.  
491 Manatt, G.J. Mauger, A.W. Meyer, T.L. Moore, E.B. Norman, B.A. Pohl, D.C. Petersen, B.  
492 Rusnak, T.B. Sundsmo, W.K. Tenbrook, R.S. Walling, Nucl. Instrum. & Methods A **569** (2006)  
493 853.  
494
- 495 3. M.-A. Descalle, D. Manatt and D. Slaughter, Lawrence Livermore Laboratory report UCRL-  
496 TR-225708 (2006).  
497
- 498 4. Varian Medical Systems, Security and Inspection, 6883 Spencer Street, Las Vegas, NV  
499 89119.  
500
- 501 5. CAARS Performance Specifications - Response to Vendors Comments, U.S. Dept. of  
502 Homeland Security, Domestic Nuclear Detection Office, Document Number DNDO PS-  
503 100380v3.00, February 2006  
504
- 505 6. M.J. Berger,<sup>1</sup> J.H. Hubbell,<sup>1</sup> S.M. Seltzer,<sup>1</sup> J. Chang,<sup>2</sup> J.S. Coursey,<sup>2</sup>  
506 R. Sukumar,<sup>2</sup> and D.S. Zucker<sup>2</sup>, XCOM: Photon Cross Sections Database, NIST Standard  
507 Reference Database 8 (XGAM), U.S. Dept. of Commerce, 1998.  
508
- 509 7. M.B. Scott, A.O. Hanson, E.M. Lyman, Phys. Rev. **84** (1951) 638.  
510
- 511 8. J.F. Briesmeister. MCNP—A General Monte Carlo N-Particle Transport Code Version 4C,  
512 Los Alamos National Laboratory (2000).  
513
- 514 9. Eljen Technology, 2010 E. Broadway, Sweetwater, Texas 79556.  
515

This work was performed under the auspices of the U. S. Department of Energy by University of California, Lawrence Livermore National Laboratory under Contract W-7405-Eng-48.